Research Square

Preprints are preliminary reports that have not undergone peer review.
They should not be considered conclusive, used to inform clinical practice,
or referenced by the media as validated information.

RAPA triggers SFN-MDM2/p53 to alleviate pulmonary fibrosis via inhibiting AECII senescence

Meiqi Liu
Chinese Academy of Medical Sciences & Peking Union Medical College
Bing Du
Capital Medical University
Ziying Xu
Capital Institute of Pediatrics
Xiaohu Cui
Chinese Academy of Medical Sciences & Peking Union Medical College
Zhoufei Li
Chinese Academy of Medical Sciences & Peking Union Medical College
Lijuan Huang
Capital Institute of Pediatrics
Jing Yuan
yuanjing6216@163.com

Chinese Academy of Medical Sciences & Peking Union Medical College

Research Article

Keywords: Idiopathic pulmonary fibrosis (IPF), rapamycin (RAPA), epithelial-mesenchymal transition (EMT), senescence

Posted Date: September 28th, 2026

DOI: https://doi.org/10.21203/rs.3.rs-10848894/v1

License: This work is licensed under a Creative Commons Attribution 4.0 International License.
Read Full License

Additional Declarations: No competing interests reported.

Abstract

Background Idiopathic pulmonary fibrosis (IPF) is a life-threatening respiratory disorder with limited therapeutic alternatives. Current approved anti-fibrotic regimens mainly target fibroblast activation, yet fail to reverse established pulmonary fibrotic lesions. Epithelial-mesenchymal transition (EMT) serves as a critical upstream driver of IPF pathogenesis, which necessitates the development of mechanism-based therapeutic strategies. This study aimed to screen FDA-approved EMT inhibitors and dissect the underlying molecular mechanisms governing lung epithelial fibrogenesis.

Methods Bioinformatic drug screening was performed using LINCS/CMAP algorithms, combined with transcriptomic analysis of human IPF clinical dataset GSE53845. Integrated transcriptomic and proteomic profiling was conducted on lung tissues from bleomycin (BLM)-challenged fibrotic mice. The BLM-induced pulmonary fibrosis mouse model was used for *in vivo* validation, and human A549 lung epithelial cells were applied for *in vitro* functional assays. We experimentally detected gene transcription, protein abundance and subcellular protein localization. All quantitative data were statistically analyzed using standard biomedical analytical approaches.

Results Rapamycin (RAPA), a clinical immunosuppressant, was identified as a robust EMT suppressor. RAPA markedly reduced SFN mRNA and protein levels in A549 cells, restored MDM2 nuclear translocation, and accelerated ubiquitin-mediated p53 degradation. This signaling cascade blocked epithelial cell senescence and ultimately slowed pulmonary fibrosis progression.

Conclusions RAPA ameliorates pulmonary fibrosis and restrains epithelial senescence by modulating the SFN-MDM2/p53 signaling axis. This work identifies an unreported anti-fibrotic regulatory pathway, and offers reliable preclinical evidence for drug repurposing of RAPA for IPF treatment.

Trial registration
No human-participant-related healthcare interventions were involved; Clinical trial number: not applicable.

Highlights

1. Rapamycin (RAPA) significantly attenuates pulmonary fibrosis induced by bleomycin and functions as a potent inhibitor of epithelial-mesenchymal transition (EMT).

2. RAPA suppress alveolar epithelial cell type II (AECII) senescence to exert anti-fibrotic effects.

3. SFN (14-3-3σ) is a key downstream mediator of RAPA, which modulates the MDM2/p53 signaling axis to regulate AECII senescence.

4. Mechanistically, SFN interacts with MDM2 to promote p53 stabilization and activation, driving cell cycle arrest, senescence, and EMT in bleomycin-induced pulmonary fibrosis.

Background

Idiopathic pulmonary fibrosis (IPF) is a progressive fibrotic interstitial lung disease of unknown cause, characterized by high mortality and limited treatment options(1). Over the past decade, the global incidence and mortality have risen, especially among the elderly(2–4). Approximately 3 million people worldwide suffer from IPF carrying a poor prognosis, and untreated patients have a median survival of 3 to 5 years(5, 6). At present, the etiology is not fully understood but may involve genetic, environmental, and immune factors (7). Thus, it's clinically important to understand IPF pathogenesis and develop effective therapies. Current treatments including antifibrotic agents like pirfenidone and nintedanib which can slow down disease progression(8), but cannot reverse lung damage(9–11). Due to the heterogeneity of patients, their therapeutic effects vary and often cause side effects that impair quality of life, emphasizing the need for new therapeutic targets and strategies(12).

Injured alveolar epithelial cells, particularly type II alveolar epithelial cells (AECII), play a central role in the development and progression of IPF(13, 14), which are essential for surfactant production and epithelial repair(15). During the early stages of IPF disease, AECII cells undergo senescence, an irreversible state that halts proliferation and promotes the release of pro-inflammatory factors, as well as epithelial-mesenchymal transition (EMT)(16, 17). EMT is a critical driver of fibrosis, transforming epithelial cells into fibroblasts that produce excessive collagen and extracellular matrix (ECM), thereby thickening lung tissue and disrupting alveolar architecture(18, 19). EMT Cells gain enhanced migratory capacity, spread throughout the lung, and further stimulate fibrosis by secreting pro-fibrotic cytokines such as transforming growth factor-β1 (TGF-β1), creating a harmful feedback loop. This process establishes a vicious cycle: epithelial injury triggers EMT, which in turn exacerbates cellular damage and accelerates disease progression(20). Although EMT inhibited -- for example, with compounds like disulfiram(19), nintedanib(21), or flavonoid Z6(22) -- can delay fibrosis, current therapies remain only modestly effective. Thus, targeting the interconnected pathways of AECII senescence and EMT remains a promising strategy for discovering new therapeutic targets in IPF.

Drug repositioning has emerged as a pivotal strategy in drug discovery, particularly for complex diseases with limited therapeutic options. By leveraging large-scale pharmacogenomic resources such as the Library of Integrated Network-based Cellular Signatures (LINCS), researchers can correlate drug-induced transcriptional profiles with disease-associated gene expression patterns, thereby identifying potential therapeutics and elucidating their mechanisms of action(23). This study utilized LINCS transcriptomic data to identify sirolimus (rapamycin, RAPA) as a drug capable of reversing bleomycin-induced EMT in A549 cells. Experimental validation demonstrated that RAPA reduces EMT and lung fibrosis in mice. By integrating mouse and patient datasets, we found that RAPA reversed senescence-associated gene expression, with SFN identified as a critical target. siRNA experiments revealed that SFN promoted senescence and EMT through the MDM2/p53 signaling pathway. Consequently, RAPA mitigates pulmonary fibrosis (PF) by targeting the SFN-MDM2/p53 axis to suppress AECII cell senescence and EMT, a mechanism corroborated by patient data. Our work not only validates an efficient computational-experimental pipeline for drug discovery, but also provides a compelling mechanistic rationale for

targeting the senescence-autophagy interplay as a promising therapeutic strategy against the fatal disease IPF.

Methods and materials

GEO database analysis

This study used lung tissue samples from patients with idiopathic pulmonary fibrosis (IPF) obtained from the GEO database. In particular, the GSE53845 dataset contains lung samples from 40 IPF patients and 8 healthy controls. After excluding samples based on gender and sample type differences, the dataset was narrowed down to 6 control subjects and 15 IPF patients for further analysis. The raw data were downloaded and normalized using the fastGEO package in R. Probe IDs were then matched to gene symbols using platform-specific annotation files. Differentially expressed marker genes were identified with the DESeq2 package, applying criteria of an adjusted p-value below 0.05 and an absolute $\log_2$ fold change greater than 1 to detect genes differentially expressed between IPF and normal lung tissues. The biological relevance of these genes was validated through a series of in vitro experiments using appropriate cell models. All computational analyses were conducted using R version 4.5.2, employing relevant R packages as needed.

LINCS+CMAP

Differentially expressed genes (DEGs) identified from a previous in vitro epithelial mesenchymal transition (EMT) model were compared with processed L1000 gene expression perturbation data from the Connectivity Map (CMAP) database(24, 25). The Connectivity Score (CS), ranging from − 1 to 1, measures the inverse relationship between small molecules and the gene expression profile of IPF. A negative CS (CS < 0) indicates that a compound may reverse EMT-related gene expression changes by downregulating genes that are upregulated and upregulating those that are downregulated, with larger absolute values reflecting greater therapeutic potential. In contrast, a positive CS (CS > 0) suggests that the compound might worsen gene expression abnormalities. The results were ranked according to the absolute CS values to identify promising drug candidates, which were then further prioritized based on their clinical applications, mechanisms of action, and safety profiles to evaluate their potential for clinical translation. The calculation and statistical analysis of the CS in the CMAP study were performed using the database's built-in algorithms, ensuring the results' reliability and reproducibility.

RNA-seq and gene set enrichment analysis

Trimomatic version 0.36 was used to remove reads that were shorter than 35 nucleotides or contained ambiguous bases. The filtered reads were then aligned to the mouse reference genome (mm10) using HISAT2. For each sample, only reads that uniquely mapped with a mapping quality score of 20 or higher were kept for further analysis. Gene-level read counts were generated using the HTSeq Python package

(version 0.9.1). Differential gene expression between treatment and control groups was analyzed with the R package limma, using a fold-change cutoff of 1.0 and a p-value threshold of 0.05. Multiple testing correction was performed using the Benjamini-Hochberg method with an alpha level of 0.05. Functional enrichment analyses of gene ontology (GO) terms and Kyoto Encyclopedia of Genes and Genomes (KEGG) pathways were conducted using the R package ClusterProfiler, considering only GO terms with p-values below 0.05.

Protein extraction and analysis

Tissue samples were ground into cell powder under liquid nitrogen and then placed into centrifuge tubes. Four times the volume of lysis buffer (8 M urea, 1% protease inhibitor cocktail) was added, followed by sonication on ice three times using a high-intensity ultrasonic processor. After digestion with trypsin, peptides were desalted using Strata X C18 SPE columns (Phenomenex) and dried under vacuum. The peptides were then dissolved in 0.5 M TEAB and processed according to the instructions for the data-independent acquisition (DIA) kit. The peptide mixtures were incubated at room temperature for two hours, combined, desalted again, and dried by vacuum centrifugation. Liver tissue samples were labeled in three batches for DIA experiments and analyzed by LC-MS/MS. The MS/MS data obtained were processed using the MaxQuant search engine (version 1.5.2.8). Mass tolerances were set at 20 ppm for precursor ions during the initial search and 5 ppm during the main search, with a fragment ion tolerance of 0.02 Da. Enrichment of differentially expressed proteins in each category was assessed using a two-tailed Fisher's exact test against the background of all identified proteins. GO terms with a corrected p-value less than 0.05 were considered significantly enriched. Furthermore, pathway enrichment analysis was performed using the KEGG database, applying a two-tailed Fisher's exact test to determine the overrepresentation of differentially expressed proteins compared to all identified proteins.

Combined Analysis of Transcriptomics and Proteomics

Differential gene expression and functional enrichment analyses were carried out following the previously established methodology. Furthermore, protein-protein interaction (PPI) networks were analyzed utilizing the STRING database.

BLM-induced PF animal model and treatment

SPF-grade male C57BL/6 mice (6–8 weeks old, 18–22 g) were purchased from Beijing Vital River Laboratory Animal Technology Co., Ltd. (strain catalogue number: VRL-C57BL/6J). All animal experiments were performed in strict accordance with the ARRIVE guidelines and the PHS Policy on Humane Care and Use of Laboratory Animals, and were approved by the Ethics Committee for Animal Experimentation at the Capital Institute of Pediatrics (approval number: DWLL2021009).

Mice were housed at six animals per cage under standardized SPF barrier conditions (20–25°C, 45%–60% relative humidity, 12 h light/dark cycle) with free access to sterilized standard rodent chow and autoclaved drinking water. All intratracheal instillation and intraperitoneal injection procedures were performed under continuous isoflurane inhalation anesthesia, and perioperative buprenorphine analgesia was applied to minimize animal suffering during modeling and drug intervention.

Animals were randomly assigned to experimental groups based on consistent age, sex and baseline body weight to balance intergroup differences. All housing, feeding, operational and temporal experimental conditions were strictly unified to eliminate confounding variables. Investigators were blinded to group allocation during sample collection, histological Ashcroft score evaluation and statistical analysis to avoid subjective bias.

Defined inclusion criteria included healthy male C57BL/6 mice aged 6–8 weeks with stable mental status and baseline body weight of 18–22 g. Mice with severe weight loss, poor vitality or accidental death before BLM treatment, as well as samples with incomplete tissue collection, were excluded from final quantitative analysis.

To establish the pulmonary fibrosis model, mice received a single intratracheal instillation of bleomycin (BLM) at doses of 1, 3, or 5 mg/kg (50 μL per mouse) on day 0, while control mice were administered an equal volume of sterile saline.

For therapeutic assessment, pulmonary fibrosis was induced by intratracheal instillation of 3 mg/kg BLM. Rapamycin (RAPA) and nintedanib (20 mg/kg) were delivered via intraperitoneal injection (10 μL/g body weight) once daily for the first week, followed by alternate-day administration until day 14.

All mice were humanely euthanized via cervical dislocation under deep isoflurane anesthesia on day 21 after BLM treatment. Isolated lung tissues were aliquoted and processed correspondingly: specimens for histology were fixed in 4% paraformaldehyde, and samples for RNA and protein analysis were snap-frozen in liquid nitrogen and stored at − 80°C. A detailed experimental timeline is presented in Fig. 1G.

Cell culture and treatment

The human lung epithelial cell line A549 was purchased from the American Type Culture Collection (ATCC, Manassas, VA, catalogue number: CCL-185, RRID: CVCL_0002). This cell line originates from a male patient and was used at passage 5–10 in all experiments. Two genetic manipulation strategies were applied in this study: transient gene knockdown mediated by small interfering RNA (siRNA), and stable SFN overexpression achieved via SFN overexpression plasmid transfection. Non-targeting siRNA and empty vector plasmid were separately utilized as matched negative controls for knockdown and overexpression groups, respectively. The parental A549 cell line is not listed on the ICLAC Register of Misidentified Cell Lines. The purchased parental cells were certified mycoplasma-negative by the ATCC supplier; routine in-house mycoplasma testing was not performed for the cultured cells in this work. The cells were cultured in Dulbecco's Modified Eagle Medium (DMEM) supplemented with 10% fetal bovine

serum (GIBCO, USA), along with penicillin G (100 U/mL) and streptomycin (100 μg/mL) (Sigma-Aldrich, USA), and maintained at 37°C in a humidified incubator with 5% CO2. A549 cells were plated at a density of 1 to 1.5 × 10^5 cells per milliliter in either 6-well or 96-well plates and allowed to attach for 24 hours. Afterward, the cells were exposed to BLM at concentrations of 2.5 μM and 5.0 μM, as well as RAPA at 50 nM, for periods of 24, 48, and 72 hours.

RNA extraction and reverse transcription - quantitative polymerase chain reaction (RT–qPCR)

Total RNA was isolated using the VeZol-Pure Total RNA Isolation Kit (Vazyme, RC202-01, China) following the manufacturer's protocol. Then, 2 μg of RNA was reverse transcribed using the PrimeScript™ RT reagent Kit with gDNA Eraser (Perfect Real Time) (Takara, RR047A, Japan). Real-time quantitative PCR was carried out on the CFX96 Touch detection system (Bio-Rad) with the SupRealQ Ultra Hunter SYBR qPCR Master Mix (U+) (Vazyme, Q713, China) and specific primers. Gene expression was measured using the comparative 2^−ΔCt method, with GAPDH as the internal control. The primer sequences used for the real-time PCR are listed in **Table S1**.

SFN knockdown and overexpression in A549 epithelial cells

Small interfering RNAs (siRNAs) targeting SFN were introduced into A549 cells to inhibit its gene expression. The siRNA sequences, obtained from GenePharm (Tsingke, China), included the following for SFN: 5'-CGAGGAGCUCUCCUGCGAATT UUCGCAGGAGAGCUCCUCGTT-3'. An SFN overexpression plasmid (SFN-OE) was purchased from Sangon Biotech (Shanghai). Cells were evenly seeded in six-well plates, and transfections were performed following the manufacturer's instructions for the Lipofectamine™ 3000 reagent (Invitrogen, USA). Subsequently, the relationship between SFN expression and lung fibrosis was assessed using real-time PCR and immunofluorescence (IF) methods.

Western blotting

Proteins were extracted from lung tissues and A549 cells using RIPA lysis buffer (Solaribio, R0010, China) with added protease and phosphatase inhibitors. Protein concentrations were measured using the bicinchoninic acid (BCA) assay (Beyotime, P0012, China). About 50 μg of each protein sample was separated by electrophoresis on a 12.5% SDS–PAGE gel (Epizyme, PG113, China). After electrophoresis, proteins were transferred onto polyvinylidene difluoride (PVDF) membranes. The membranes were blocked with QuickBlock™ Blocking Buffer for Western Blot (Beyotime, P0252, China) for 45 minutes at room temperature, then incubated overnight at 4°C with primary antibodies. Cytoplasmic and nuclear protein fractions were extracted using the Cytoplasmic-protein/Nucleoprotein/Histone Extraction Kit (Bailaibo Technology, Beijing, China; Cat. No. HR0041) following the manufacturer's instructions. The primary antibodies used were Vimentin (1:1000, Cell Signaling Technology, 5741T, USA), α-SMA (1:1000, Abcam, AB124964, UK), 14-3-3σ (1:10000, Proteintech, 66251-1-Ig, China), p53 (1:1000, Abcam, AB26, UK), ATM (1:10000, Proteintech, 83608-5-RR, China), phospho-p53 (Ser15) (1:6000, Proteintech, 67826-1-

Ig, China), Mdmd2 (1:3000, Proteintech, 27883-1-AP, China), Lamin B1 (1:30000, Bioss Antibodies, bsm-52361R, China), and Actin (1:1000, Abcam, ab179467, UK). Afterwards, membranes were incubated with horseradish peroxidase (HRP)-linked secondary antibodies (1:5000) at room temperature for one hour. Following three washes with TBST (10 minutes each), protein bands were visualized using 200 μL of Ultra-sensitive ECL Chemiluminescence Kit (Beyotime, P0018S, China) and imaged with a ChemiDoc™ Imaging System (Bio-Rad Laboratories, Hercules, CA, USA). Band intensities were analyzed using ImageJ software (National Institutes of Health, Bethesda, MD, USA). All Western blot assays were conducted in triplicate, and protein expression levels were normalized to Actin as the internal loading control.

Immunofluorescence (IF) staining

A549 cells and lung tissue samples were fixed with 4% paraformaldehyde (PFA) for 10 minutes, then washed with phosphate-buffered saline (PBS) and permeabilized using 0.3% Triton X-100 for 15 minutes. The samples were blocked with Immunol Staining Blocking Buffer (Beyotime, P0102, China) for one hour. Afterwards, the cells were incubated overnight at 4°C with primary antibodies including Vimentin (1:200, Cell Signaling Technology, 5741T, USA), α-SMA (1:200, Abcam, AB124964, UK), E-cadherin (1:500, Proteintech, 20874-1-AP, China), 14-3-3σ (1:500, Proteintech, 66251-1-Ig, China), p53 (1:500, Abcam, AB26, UK), ATM (1:500, Proteintech, 83608-5-RR, China), and phospho-p53 (Ser15) (1:500, Proteintech, 67826-1-Ig, China). After three washes with PBS for 5 minutes each to remove unbound antibodies, the cells were incubated for one hour at room temperature with either Cy3-conjugated Goat Anti-Mouse IgG Antibody (H + L) (1:500, Bioss, bs-0296G-Cy3, USA) or FITC-conjugated Goat Anti-Rabbit IgG Antibody (H + L) (1:500, Bioss, bs-0295D-FITC, USA). Following further PBS washes, nuclei were stained with Hoechst 33342 (MCE, USA). Fluorescent images of the stained cells were then captured using a KEYENCE BZ-X series all-in-one fluorescence microscope imaging system (KEYENCE, Japan).

CCK-8 Assay

Cell viability was assessed using the Cell Counting Kit-8 (CCK-8) kit (DOJINDO, China) following the manufacturer's instructions. Cells were exposed to specified concentrations of BLM and RAPA for 24, 48, and 72 hours. After treatment, cells were rinsed with phosphate-buffered saline (PBS), and the detection solution was prepared by combining 90 μL of PBS with 10 μL of CCK-8 reagent per well. The plates were incubated in the dark for 30 minutes. Optical density (OD) was then measured at 450 nm using a microplate reader, and the results were collected for further analysis.

H&E Staining

Lung tissue samples from the right upper lobe were collected, fixed in 4% paraformaldehyde, and embedded in paraffin. Sections of 4 μm thickness were prepared and stained using standard hematoxylin and eosin protocols. Specifically, sections were stained with hematoxylin at room temperature for 5 minutes, rinsed under running water for 30 seconds, then stained with eosin at room temperature for 15 minutes, followed by another rinse with running water. The stained sections were dehydrated through graded alcohols and xylene, cleared with neutral resin, and examined under a light microscope with a 20x objective to evaluate tissue morphology.

Masson’s Trichrome Staining

Mouse lung tissue sections were treated with Bouin’s solution at 56°C for one hour, then sequentially stained with Mayer’s hematoxylin for 5 minutes, Biebrich scarlet-acid fuchsin for 10 minutes, phosphomolybdic acid-phosphotungstic acid for 15 minutes, and aniline blue for 2 hours. All staining reagents were sourced from Sigma-Aldrich. The stained sections were observed using light microscopy.

SA-β-Galactosidase Staining

Senescent cells were detected using senescence-associated β-galactosidase (SA-β-gal) staining. Cells grown in 96-well plates were washed, fixed, and stained following the instructions of the SA-β-gal cellular senescence assay kit (Absin, China) and established protocols. The stained cells were then examined under a microscope.

Statistical Analysis

All quantitative data are presented as mean ± standard error of the mean (SEM). The biological replicate number (n) for every experimental group is indicated in each figure legend. Independent biological replicates were repeated to confirm all experimental phenotypes, while technical replicates were included to guarantee measurement stability. All results were fully reproducible across repeated independent trials, and no non-replicable data were identified in this work.

Statistical calculations were performed with GraphPad Prism 9.0 software. For datasets governed by a single experimental factor, intergroup differences were assessed via two-sided ordinary one-way analysis of variance (ANOVA), followed by two-sided post hoc Student’s t-tests for pairwise subgroup comparisons. For datasets containing two independent experimental variables, two-way ANOVA was adopted to evaluate the main effects of each factor as well as their interaction effect, with two-sided pairwise t-tests for post-hoc comparisons between groups. Survival curve disparities were evaluated via two-sided log-rank test. All statistical tests conducted in this study were two-sided. Statistical significance was defined as $p < 0.05$, with asterisks marked within figures to denote distinct significance levels: *$p < 0.05$, **$p < 0.01$, ***$p < 0.001$.

Results

Rapamycin potently inhibits bleomycin-induced epithelial mesenchymal transition and attenuates pulmonary fibrosis

To screen for compounds capable of reversing EMT, we performed computational drug repositioning using the Connectivity Map (CMAP)/LINCS algorithm. By comparing the gene expression signature of BLM-induced EMT with compound-perturbed transcriptomic profiles, we selected candidates with a negative connectivity score (CS) and $P < 0.05$, indicating an inverse regulatory relationship. Notably, among the 10 shortlisted candidate drugs, the mTOR inhibitor rapamycin (RAPA) displayed the most

significantly negative CS, suggesting a robust antagonistic effect against EMT (Fig. 1A). In contrast, the autophagy inhibitor sunitinib exhibited a positive CS, providing biological support for the reliability of our screening strategy (**Table S2 and S3**). Thus, RAPA, a well-established agent with anti-tumor and anti-aging properties(26), holds great potential as a therapeutic candidate for IPF.

Next, to identify potential therapeutic agents targeting epithelial-mesenchymal transition (EMT) in PF, we established an in *vitro* EMT model in A549 alveolar epithelial cells stimulated with bleomycin (BLM). Treatment with 5.0 μM BLM significantly reduced cell viability in a dose-dependent manner, accompanied by increased expression of the mesenchymal marker fibronectin and decreased expression of the tight junction protein zonula occludens-1 (ZO-1) (**Fig. S1A and S1B**). Further mechanistic exploration was conducted at the transcriptomic level based on the *in vitro* EMT model, Venn diagram analysis screened the overlapping differentially expressed genes (DEGs) shared by the BLM-triggered EMT model and RAPA-treated cells (Fig. 1B). Kyoto Encyclopedia of Genes and Genomes (KEGG) pathway enrichment further revealed that 138 inversely regulated genes were highly enriched in cell adhesion, autophagy, cell cycle progression, and endoplasmic reticulum protein processing—all core pathways closely associated with EMT (Fig. 1C). Functional validation confirmed that RAPA markedly suppressed BLM-induced upregulation of vimentin and α-smooth muscle actin (α-SMA) at 24, 48, and 72 h (Fig. 1D and 1E), while restoring the expression of *Fibronectin* and *ZO-1* (Fig. 1F). Our results indicated that RAPA could effectively inhibit EMT progression.

Also, the above findings were additionally validated in a murine BLM-induced pulmonary fibrosis (PF) model, and its therapeutic potency was compared with that of the clinically established drug nintedanib. Dose-escalation experiments showed that 5 mg/kg BLM caused early lethality, whereas 3 mg/kg BLM consistently induced severe fibrosis without excessive mortality (**Fig. S2A and S2B**). Mice treated with 3 mg/kg BLM exhibited significant upregulation of *Collagen I*, *α-SMA*, and *Vimentin*, together with downregulation of the epithelial marker *E-cadherin* (**Fig. S2C**). Histopathological examination confirmed extensive alveolar destruction, inflammatory infiltration, and collagen deposition (**Fig. S2D and S2E**). To evaluate the therapeutic efficacy of RAPA, BLM-challenged mice were administered 2 mg/kg RAPA according to the protocol shown in Fig. 1G. RAPA treatment significantly improved survival compared with the BLM group (Fig. 1H) and normalized the expression of fibrotic and EMT-related markers in lung tissues (Fig. 1I). Importantly, RAPA markedly attenuated BLM-induced lung structural damage, inflammatory cell infiltration, and extracellular matrix deposition, as revealed by H&E and Masson's trichrome staining (Fig. 1J and 1K). Notably, intraperitoneally delivered Nintedanib exerted comparable therapeutic effects on survival rate and extracellular matrix (ECM) deposition in BLM-induced pulmonary fibrosis mice when compared with 2 mg/kg RAPA (Fig. 1H, 1I, 1J and 1K). For EMT-related molecular profiles, both RAPA and Nintedanib significantly reduced the mRNA levels of *Collagen I* and *Tgfb1*, while markedly elevating the mRNA expression of *E-cadherin* in lung tissues of BLM-challenged mice. Additionally, although both agents decreased BLM-triggered upregulation of *vimentin* mRNA expression, this change did not reach statistical significance in the nintedanib group (Fig. 1I).

RAPA attenuates pulmonary fibrosis by suppressing alveolar epithelial cell senescence revealed by integrated multi-omics analyses

To delineate the molecular mechanisms by which RAPA mitigates idiopathic pulmonary fibrosis (IPF), we treated BLM-induced IPF mice with RAPA and performed by analyzing integrated transcriptomic and proteomic profiling of mouse lung tissues.

The results showed that BLM-induced PF mice elicited extensive transcriptomic (**Fig. S3A and S3B**) and proteomic (**Fig. S3C**) perturbations. KEGG (**Fig. S3E**) and Gene Ontology (GO) (**Fig. S3F**) enrichment analyses revealed dysregulation of pathways associated with DNA damage response, p53 signaling, and mitochondrial dysfunction, which was accompanied by aberrant expression of the senescence regulators *SFN* and *CDKN1A*. Importantly, RAPA significantly reversed these pathological alterations: KEGG (Fig. 2A) and GO (Fig. 2B) enrichment analyses confirmed that RAPA restored G1/S cell cycle transition, mitochondrial homeostasis, and p53 signaling balance, thereby re-establishing metabolic equilibrium. BLM challenge significantly increased senescence scores and senescence-associated secretory phenotype (SASP) expression in mouse lung tissues, which were markedly suppressed by RAPA treatment (Fig. 2C). Furthermore, KEGG and GO enrichment analyses of the human IPF dataset GSE53845 (**Fig. S3G**) validated the activation of senescence- and fibrosis-related pathways in clinical IPF samples, underscoring the translational relevance of our findings.

In A549 cells, RAPA attenuated BLM-induced senescence-associated β-galactosidase (SA-β-gal) positivity (Fig. 2D), upregulation of p21 protein and *CDKN1A* mRNA (Fig. 2E), as well as DNA damage (γH2AX accumulation) and p21 overexpression (Fig. 2F). A time-dependent reduction in γH2AX (**Fig. S4A and S4B**) and p21 (**Fig. S4C and S4D**) levels was also observed following RAPA intervention. Consistent with these findings, *CDKN1A* expression was significantly higher in IPF patients compared to healthy controls (Fig. 2G). In summary, these observations demonstrate that AECII senescence drives PF, and RAPA mediates its anti-fibrotic effects via the inhibition of AECII senescence.

Flow cytometry analysis demonstrated that compared with the control group, BLM treatment induced a robust, time-dependent G2/M phase arrest accompanied by a significant reduction in the G1-phase population. Importantly, compared with the BLM group, RAPA co-treatment effectively reversed this BLM-triggered G2/M arrest, restoring the cell cycle distribution to a pattern comparable to the control group at all three time points (**Fig. S4E, S4F and S4G**).

SFN (14-3-3σ) serves as a key target underlying the anti-fibrotic and anti-senescent effects of rapamycin

To identify critical molecular targets responsible for the therapeutic effects of RAPA, we constructed two (protein–protein interaction) PPI networks using integrated transcriptomic and proteomic data: one for DEGs from BLM versus control (Fig. 3A), and another for DEGs from BLM+RAPA versus BLM (**Fig. S3D**).

No genes exhibited concordant changes at both mRNA and protein levels between the BLM and BLM+RAPA groups (**Fig. S3D**). In contrast, PPI analysis of the BLM versus control cohort (Fig. 3A) screened a set of core co-regulated genes. The identified candidates included alveolar epithelial cell-enriched *SFN*, *PHPT1*, *PARD3* and *NT5C*, as well as macrophage-expressed *APOE* and T cell-associated *SNTA1*.

We further validated the expression patterns of these epithelial-related candidates in A549 cells and the human IPF dataset GSE53845. Among them, only *SFN* and *PARD3* displayed consistent regulatory responses: BLM markedly upregulated their expression, whereas RAPA treatment efficiently reversed this induction (Fig. 3B). The expression profiles of *SFN*, *PHPT1* and *PARD3* in human IPF lung tissues were highly consistent with those observed in mouse models (Fig. 3C). *SFN* encodes 14-3-3σ, which modulates cell cycle progression and cellular senescence by governing the MDM2/p53 signaling pathway. Intriguingly, BLM triggered robust *SFN* mRNA induction as early as 6 and 12 h, indicating an early transcriptional activation of *SFN* at the initial stage of fibrogenesis; this upregulation was markedly abrogated by RAPA (Fig. 3F). Moreover, RAPA effectively suppressed BLM-induced 14-3-3σ protein upregulation in mouse lung tissues (Fig. 3D), as well as in A549 cells at multiple time points (Fig. 3E, 3F and 3G).

Collectively, these findings demonstrate that *SFN* (14-3-3σ) acts as a pivotal molecular target mediating the anti-fibrotic and anti-senescent actions of RAPA in BLM-induced PF.

SFN acts as an essential upstream mediator of rapamycin in regulating BLM-induced AECII senescence, EMT and p53/DNA damage signaling

SFN serves as an essential mediator enabling RAPA to alleviate BLM-triggered AECII senescence and EMT. To validate the regulatory role of *SFN* in BLM-induced EMT and cellular senescence, we performed loss- and gain-of-function assays in A549 cells. In *SFN* knockdown experiments, depletion of *SFN* markedly blunted BLM-induced upregulation of *SFN*, *Fibronectin*, and *CDKN1A* mRNA levels (Fig. 4A). *SFN* silencing also significantly reduced the BLM-evoked ratio of SA-β-gal-positive senescent cells (Fig. 4B) and suppressed the induction of vimentin and p21 protein expression (Fig. 4C and 4D). Additionally, *SFN* knockdown notably inhibited the increase in 14-3-3σ fluorescence intensity upon BLM stimulation (Fig. 4E).

In *SFN* overexpression rescue assays, RAPA treatment effectively reversed the elevated expression of 14-3-3σ induced by *SFN* overexpression (Fig. 4F). Consistently, RAPA normalized the increased mRNA levels of *SFN*, *Fibronectin*, and *CDKN1A* (Fig. 4G) and restored the excessive SA-β-gal activity caused by *SFN* overexpression (Fig. 4H). Moreover, RAPA abrogated the pro-EMT and pro-senescence effects of *SFN* overexpression, as evidenced by decreased vimentin and p21 fluorescence signals (Fig. 4I and 4J). Further immunofluorescence (IF) validation confirmed the regulatory effect of *SFN* on BLM-induced EMT at both 24 h and 48 h (**Fig. S5A, S5B, S5C and S5D**).

Mechanistically, *SFN* was required for the activation of p53 signaling and DNA damage-dependent p53 activation. In *SFN*-knockdown A549 cells, BLM-induced upregulation of γH2AX, ATM, phospho-p53 (Ser15), p53, and MDM2 was prominently alleviated (Fig. 5A, 5B, 5C, 5D and 5E). In *SFN* overexpression rescue experiments, RAPA intervention effectively reversed the enhanced activation of these DNA damage and p53 pathway molecules triggered by *SFN* overexpression (Fig. 5F, 5G, 5H, 5I and 5J).

RAPA reverses BLM-induced activation of the MDM2/p53 signaling axis and ATM-mediated DNA damage signaling

To further elucidate the mechanism by which *SFN* modulates the p53 pathway, we focused on MDM2, a key E3 ubiquitin ligase that governs p53 protein stability, nucleocytoplasmic shuttling, and proteasomal degradation.

In A549 cells, BLM stimulation significantly perturbed the subcellular localization of 14-3-3σ, MDM2 and p53: 14-3-3σ and MDM2 accumulated predominantly in the cytoplasm (Fig. 6A and 6E), whereas p53 was largely sequestered in the nucleus (Fig. 6B and 6E). Additionally, co-localization analysis at 72 h post-BLM treatment revealed an interaction between 14-3-3σ and MDM2 (Fig. 6F). Notably, RAPA co-treatment effectively reversed these BLM-induced perturbations, restoring the balanced subcellular distribution of MDM2 and p53 (Fig. 6A, 6B, and 6E).

We further examined the transcriptional levels of *TP53* and *MDM2* in A549 cells at 24, 48, and 72 h post-treatment. BLM did not significantly alter *TP53* mRNA expression but prominently upregulated *MDM2* transcription. In contrast, RAPA intervention significantly increased *TP53* mRNA levels while downregulating *MDM2* mRNA at 24 and 48 h, confirming its regulatory role at the transcriptional level (Fig. 6C). However, at the protein level, BLM treatment increased the total protein abundance of p53 and Mdm2 in A549 cells, and these alterations were reversed upon RAPA co-treatment (Fig. 6D). Clinical validation using the GSE53845 IPF dataset demonstrated that transcript levels of *TP53* and *MDM2* were markedly elevated in lung tissues from IPF patients compared to healthy controls, underscoring the translational relevance of our findings (Fig. 6G).

As ATM kinase acts as a core DNA-damage sensor, BLM-induced DNA damage triggers ATM activation and subsequent p53 phosphorylation at Ser15. We therefore explored the ATM-phospho-p53 (Ser15) signaling cascade. Western blot analysis of whole-cell lysates from A549 cells collected at 24, 48 and 72 h post-BLM stimulation showed elevated total protein levels of total ATM and phospho-p53 (Ser15). All these DNA-damage-driven molecular alterations were substantially mitigated by RAPA co-treatment (Fig. 6H). Supporting immunofluorescence staining at 24 h further validated this regulatory pattern, wherein RAPA suppressed BLM-triggered enhancement of total ATM (green) and Ser15-p53 (red) fluorescence intensity (Fig. 6I).

Taken together, BLM activates p53 signaling through a dual regulatory mechanism: (1) triggering a DNA damage response to promote ATM-mediated phosphorylation of p53 at Ser15; (2) altering MDM2

subcellular localization (cytoplasmic accumulation) and facilitating its interaction with 14-3-3σ to sustain nuclear p53 accumulation and stability. RAPA efficiently counteracts BLM-induced p53 pathway activation at the transcriptional, post-translational, and subcellular distribution levels (Fig. 7).

Discussion

Pulmonary fibrosis (PF), particularly idiopathic pulmonary fibrosis (IPF), is a progressive and fatal interstitial lung disease(27, 28). In recent years, the pathogenic paradigm of IPF has shifted from chronic inflammation to repetitive alveolar epithelial damage, abnormal fibroblast activation and dysregulated extracellular matrix (ECM) remodeling(15, 29). Meanwhile, emerging mechanisms including cellular senescence, mitochondrial dysfunction and epigenetic regulation have also been widely recognized.(30–32)—its clinical management still faces severe bottlenecks(33, 34). Although high-resolution CT (HRCT) and novel biomarkers such as KL-6 and MMP-7 have facilitated diagnosis, early screening of IPF is still difficult(35–37). Current first-line anti-fibrotic drugs, nintedanib and pirfenidone, can only delay rather than reverse the decline in lung function and are associated with side effects(38). Moreover, most clinical trials targeting the TGF-β1 pathway have yielded unsatisfactory outcomes(39, 40). Lung transplantation is limited by donor availability and carries high risks and costs. Moreover, most clinical trials targeting the TGF-β1 pathway have yielded unsatisfactory outcomes.

Given the above challenges, this study targeted type II alveolar epithelial cell (AECII) senescence, an upstream pathological event in PF initiation and progression(41–43). Persistent sublethal injury to AECII is well-established as the primary trigger of IPF(14, 41, 44). Senescent AECII create a self-amplifying pro-fibrotic microenvironment through the secretion of the senescence-associated secretory phenotype (SASP), which directly drives epithelial-mesenchymal transition (EMT) and extracellular matrix deposition, forming a vicious cycle(13, 14, 45, 46). Drug repurposing has become a cost-effective and efficient strategy for drug development for intractable diseases. Herein, combining LINCS database computational prediction with in vitro and in vivo experimental verification, we demonstrated that the mTOR inhibitor rapamycin (RAPA, sirolimus) exerts potent anti-EMT and antifibrotic activities in PF models. On this basis, we further explored whether RAPA alleviates PF via suppressing AECII senescence.

Integrated transcriptomic and proteomic analyses revealed that bleomycin (BLM)-induced PF is accompanied by sustained activation of the DNA damage-p53 axis, cell cycle arrest and mitochondrial dysfunction, all hallmark characteristics of cellular senescence. Notably, RAPA treatment effectively reversed these pathological molecular alterations across mouse models and clinical IPF samples. Further screening identified stratifin (SFN/14-3-3σ) as a core effector molecule. SFN is an epithelium-enriched cell cycle checkpoint protein(47, 48). Consistent across cellular, murine PF models and clinical IPF tissues, SFN expression was markedly elevated during fibrogenesis and positively correlated with disease severity. Functional assays confirmed that SFN acts as a positive regulator of AECII senescence: SFN knockdown alleviated cellular senescence, whereas SFN overexpression was sufficient to trigger senescent phenotypes.

We next dissected the molecular mechanism by which SFN modulates p53 signaling via the E3 ubiquitin ligase MDM2(49). Under fibrotic conditions, upregulated SFN interacts with MDM2 and retains MDM2 in the cytoplasm, which blocks the nuclear translocation of MDM2(50). As a result, nuclear p53 cannot be efficiently ubiquitinated and degraded, leading to abnormal p53 accumulation and activation in the nucleus. Meanwhile, BLM-induced DNA damage activates ATM kinase, which phosphorylates p53 at Ser15 and further enhances the transcriptional activity of p53. The combined effects of these two events upregulate downstream senescence-related genes such as p21, ultimately inducing cell cycle arrest and AECII senescence.

Mechanistically, RAPA exerts its protective effects by downregulating SFN expression. Reduced SFN releases sequestered MDM2, restores MDM2 nuclear distribution and its physiological function to degrade p53. Additionally, RAPA suppresses ATM-dependent p53 (Ser15) phosphorylation, thereby reversing AECII senescence and the subsequent profibrotic cascade. Notably, previous studies mainly focused on the roles of SFN (14-3-3σ) in tumor progression(51–53) and DNA damage response(54, 55). Our work firstly clarifies the SFN-MDM2/p53 axis in regulating AECII senescence during pulmonary fibrosis, expanding the biological function of SFN in fibrotic diseases.

The major contribution of the present study is the establishment and validation of a complete signaling cascade: RAPA induced SFN downregulation → restored MDM2 nuclear function and p53 degradation → inhibited AECII senescence and SASP release → alleviated EMT and pulmonary fibrosis. Loss- and gain-of-function assays confirmed that SFN is an indispensable downstream mediator for the anti-senescence and antifibrotic effects of RAPA. This finding goes beyond the canonical function of RAPA as an mTORC1 inhibitor, and provides a novel molecular mechanism for its antifibrotic action dependent on AECII senescence regulation.

This study has several limitations. Mechanistic experiments were conducted in the A549 cell line and bleomycin-induced mouse model, which cannot fully recapitulate human IPF; further validation in primary human AECII and large clinical cohorts is needed. The binding domains of SFN-MDM2 and the mTORC1-independent mechanism of RAPA regulating SFN also remain to be clarified. Future work will focus on patient stratification for precision therapy, development of SFN-MDM2 interaction inhibitors, and combined treatment strategies to optimize anti-fibrotic efficacy.

Conclusion

This study elucidates a new mechanism whereby rapamycin (RAPA) relieves pulmonary fibrosis (PF) via the SFN-MDM2/p53 axis. In fibrotic conditions, elevated SFN traps MDM2 in the cytoplasm, while DNA damage activates ATM-p53 signaling; together they trigger AECII senescence. RAPA reduces SFN expression to restore p53 turnover and reverse profibrotic senescent phenotypes. Our findings expand the understanding of PF pathogenesis, reveal an mTOR-independent antifibrotic action of RAPA, and highlight SFN as a viable therapeutic target.

Abbreviations

AECII
type II alveolar epithelial cells
BLM
bleomycin
CCK-8
Cell Counting Kit-8
CMAP
Connectivity Map
ECM
extracellular matrix
EMT
epithelial-mesenchymal transition
GO
Gene Ontology
IF
immunofluorescence
IPF
idiopathic pulmonary fibrosis
KEGG
Kyoto Encyclopedia of Genes and Genomes
LINCS
Library of Integrated Network-based Cellular Signatures
PF
pulmonary fibrosis
PPI
protein-protein interaction
PVDF
polyvinylidene difluoride
RAPA
Rapamycin (Sirolimus)
RT-qPCR
reverse transcription-quantitative polymerase chain reaction
SA-β-gal
senescence-associated β-galactosidase
SASP
senescence-associated secretory phenotype
siRNA
small interfering RNA

α-SMA
α-smooth muscle actin
TGF-β1
transforming growth factor-β1
ZO-1
zonula occludens-1.

Declarations

Ethics approval statement

The animal study protocol received formal approval from the Institutional Animal Care and Use Committee of Children's Hospital, Capital Institute of Pediatrics (Ethics filing reference No. SHERDWLL, approval No. DWLL2023020, approved on December 14, 2023). All mouse experiments were carried out in strict compliance with the International Council for Laboratory Animal Science (ICLAS) guidelines and institutional animal care regulations.

Consent for publication

This manuscript does not involve any individual human data, clinical images or patient-related materials. Thus, consent for publication is not applicable.

Competing interests

The authors declare that they have no competing interests.

Funding Statement

Financial support for this study was provided by the National Natural Science Foundation of China (Grant No. 82372270).

Author Contribution

Meiqi Liu and Bing Du designed the research framework, performed in vivo animal experiments, cell functional assays, molecular detection and bioinformatics analysis, drafted and revised the original manuscript; Ziying Xu participated in cell culture and molecular phenotype verification; Xiaohu Cui and Zhoufei Li collected experimental data and conducted statistical analysis; Lijuan Huang supervised the whole project, validated molecular mechanism, reviewed and edited the manuscript; Jing Yuan

conceived and administrated this study, acquired research funding, finalized the manuscript. All authors read and approved the final submitted manuscript.

Acknowledgement

All authors appreciate the experimental technical support offered by the laboratory staff. No individuals who fail to meet the authorship criteria contributed to this work.

Data Availability

The human IPF transcriptome dataset GSE53845 analyzed in this study was retrieved from the public Gene Expression Omnibus (GEO) repository. Transcriptome expression matrices (FPKM normalized) and normalized proteome matrices (LFQ intensity from label free proteomics) are provided in the supplementary materials. Processed analytical datasets, unprocessed imaging and Western blot raw data are provided within the manuscript and Supplementary Information for reference.

References

1. Collard HR, Ryerson CJ, Corte TJ, Jenkins G, Kondoh Y, Lederer DJ, et al. Acute Exacerbation of Idiopathic Pulmonary Fibrosis. An International Working Group Report. Am J Respir Crit Care Med. 2016;194:265–75. 10.1164/rccm.201604-0801CI.
2. Cox IA, Otahal P, de Graaff B, Corte TJ, Moodley Y, Zappala C, et al. Incidence, prevalence and mortality of idiopathic pulmonary fibrosis in Australia. Respirology. 2022;27:209–16. 10.1111/resp.14194.
3. Hutchinson J, Fogarty A, Hubbard R, McKeever T. Global incidence and mortality of idiopathic pulmonary fibrosis: a systematic review. Eur Respir J. 2015;46:795–806. 10.1183/09031936.00185114.
4. Liu Y, Zhu M, Geng J, Ban C, Zhang S, Chen W, et al. Incidence and radiologic-pathological features of lung cancer in idiopathic pulmonary fibrosis. Clin Respir J. 2018;12:1700–5. 10.1111/crj.12732.
5. Luppi F, Kalluri M, Faverio P, Kreuter M, Ferrara G. Idiopathic pulmonary fibrosis beyond the lung: understanding disease mechanisms to improve diagnosis and management. Respir Res. 2021;22:109. 10.1186/s12931-021-01711-1.
6. León-Román F, Valenzuela C, Molina-Molina M. Idiopathic pulmonary fibrosis. Med Clin (Barc). 2022;159:189–94. 10.1016/j.medcli.2022.02.020.
7. Munchel JK, Shea BS. Diagnosis and Management of Idiopathic Pulmonary Fibrosis. R I, Med J. (2013). 2021;104:26–9.
8. Homma S, Suda T, Hongo Y, Yoshida M, Hiroi S, Iwasaki K, et al. Incidence and changes in treatment of acute exacerbation of idiopathic pulmonary fibrosis in Japan: A claims-based retrospective study.

Respir Investig. 2022;60:798–805. 10.1016/j.resinv.2022.07.004.

9. Salisbury ML, Wijsenbeek MS. Management of Idiopathic Pulmonary Fibrosis. Clin Chest Med. 2021;42:275–85. 10.1016/j.ccm.2021.03.004.
10. Koudstaal T, Wijsenbeek MS. Idiopathic pulmonary fibrosis. Presse Med. 2023;52:104166. 10.1016/j.lpm.2023.104166.
11. Podolanczuk AJ, Thomson CC, Remy-Jardin M, Richeldi L, Martinez FJ, Kolb M, et al. Idiopathic pulmonary fibrosis: state of the art for 2023. Eur Respir J. 2023;61. 10.1183/13993003.00957-2022.
12. Mullholand JB, Grossman CE, Perelas A. Non-Pharmacological Management of Idiopathic Pulmonary Fibrosis. J Clin Med. 2025;14. 10.3390/jcm14041317.
13. Parimon T, Chen P, Stripp BR, Liang J, Jiang D, Noble PW, et al. Senescence of alveolar epithelial progenitor cells: a critical driver of lung fibrosis. Am J Physiol Cell Physiol. 2023;325:C483–95. 10.1152/ajpcell.00239.2023.
14. Parimon T, Yao C, Stripp BR, Noble PW, Chen P. Alveolar Epithelial Type II Cells as Drivers of Lung Fibrosis in Idiopathic Pulmonary Fibrosis. Int J Mol Sci. 2020;21. 10.3390/ijms21072269.
15. Moss BJ, Ryter SW, Rosas IO. Pathogenic Mechanisms Underlying Idiopathic Pulmonary Fibrosis. Annu Rev Pathol. 2022;17:515–46. 10.1146/annurev-pathol-042320-030240.
16. Adams TS, Schupp JC, Poli S, Ayaub EA, Neumark N, Ahangari F et al. Single-cell RNA-seq reveals ectopic and aberrant lung-resident cell populations in idiopathic pulmonary fibrosis. Sci Adv. 2020;6:eaba1983; 10.1126/sciadv.aba1983.
17. Habermann AC, Gutierrez AJ, Bui LT, Yahn SL, Winters NI, Calvi CL et al. Single-cell RNA sequencing reveals profibrotic roles of distinct epithelial and mesenchymal lineages in pulmonary fibrosis. Sci Adv. 2020;6:eaba1972; 10.1126/sciadv.aba1972.
18. Zhang C, Zhu X, Hua Y, Zhao Q, Wang K, Zhen L, et al. YY1 mediates TGF-β1-induced EMT and pro-fibrogenesis in alveolar epithelial cells. Respir Res. 2019;20:249. 10.1186/s12931-019-1223-7.
19. Wu X, Xu H, Zhang Z, Ma Z, Zhang L, Wang C, et al. Disulfiram Alleviates MTX-Induced Pulmonary Fibrosis by Inhibiting EMT in Type 2 Alveolar Epithelial Cells. Lung. 2024;203:4. 10.1007/s00408-024-00764-5.
20. Feng J, Huang X, Peng Y, Yang W, Yang X, Tang R, et al. Pyruvate kinase M2 modulates mitochondrial dynamics and EMT in alveolar epithelial cells during sepsis-associated pulmonary fibrosis. J Transl Med. 2025;23:205. 10.1186/s12967-025-06199-7.
21. Ihara H, Mitsuishi Y, Kato M, Takahashi F, Tajima K, Hayashi T, et al. Nintedanib inhibits epithelial-mesenchymal transition in A549 alveolar epithelial cells through regulation of the TGF-β/Smad pathway. Respir Investig. 2020;58:275–84. 10.1016/j.resinv.2020.01.003.
22. Gao Z, Xu M, Liu C, Gong K, Yu X, Lu K, et al. Structural Modification and Optimisation of Hyperoside Oriented to Inhibit TGF-β-Induced EMT Activity in Alveolar Epithelial Cells. Pharmaceuticals (Basel). 2024;17. 10.3390/ph17050584.

23. Koleti A, Terryn R, Stathias V, Chung C, Cooper DJ, Turner JP, et al. Data Portal for the Library of Integrated Network-based Cellular Signatures (LINCS) program: integrated access to diverse large-scale cellular perturbation response data. Nucleic Acids Res. 2018;46:D558–66. 10.1093/nar/gkx1063.
24. Marino GB, Evangelista JE, Clarke DJB, Ma'ayan A. L2S2: chemical perturbation and CRISPR KO LINCS L1000 signature search engine. Nucleic Acids Res. 2025;53:W338–50. 10.1093/nar/gkaf373.
25. Barkhaus PE, Nandedkar SD, de Carvalho M, Swash M, Stålberg EV. Revisiting the compound muscle action potential (CMAP). Clin Neurophysiol Pract. 2024;9:176–200. 10.1016/j.cnp.2024.04.002.
26. Blagosklonny MV. Cancer prevention with rapamycin. Oncotarget. 2023;14:342–50. 10.18632/oncotarget.28410.
27. Raghu G, Remy-Jardin M, Myers JL, Richeldi L, Ryerson CJ, Lederer DJ, et al. Diagnosis of Idiopathic Pulmonary Fibrosis. An Official ATS/ERS/JRS/ALAT Clinical Practice Guideline. Am J Respir Crit Care Med. 2018;198:e44–68. 10.1164/rccm.201807-1255ST.
28. King TE Jr., Bradford WZ, Castro-Bernardini S, Fagan EA, Glaspole I, Glassberg MK, et al. A phase 3 trial of pirfenidone in patients with idiopathic pulmonary fibrosis. N Engl J Med. 2014;370:2083–92. 10.1056/NEJMoa1402582.
29. Wolters PJ, Collard HR, Jones KD. Pathogenesis of idiopathic pulmonary fibrosis. Annu Rev Pathol. 2014;9:157–79. 10.1146/annurev-pathol-012513-104706.
30. Kellogg DL, Kellogg DL Jr., Musi N, Nambiar AM. Cellular Senescence in Idiopathic Pulmonary Fibrosis. Curr Mol Biol Rep. 2021;7:31–40. 10.1007/s40610-021-00145-4.
31. Bueno M, Calyeca J, Rojas M, Mora AL. Mitochondria dysfunction and metabolic reprogramming as drivers of idiopathic pulmonary fibrosis. Redox Biol. 2020;33:101509. https://doi.org/10.1016/j.redox.2020.101509.
32. Li X, Feng C, Peng S. Epigenetics alternation in lung fibrosis and lung cancer. Front Cell Dev Biol. 2022;10:1060201. 10.3389/fcell.2022.1060201.
33. Bando M, Chiba H, Miyazaki Y, Suda T. Current challenges in the diagnosis and management of idiopathic pulmonary fibrosis in Japan. Respir Investig. 2024;62:785–93. 10.1016/j.resinv.2024.06.006.
34. Muri J, Durcová B, Slivka R, Vrbenská A, Makovická M, Makovický P, et al. Idiopathic Pulmonary Fibrosis: Review of Current Knowledge. Physiol Res. 2024;73:487–97. 10.33549/physiolres.935322.
35. Kayıkçı A, Alatas F, Alatas IO, Yıldırım H, Ozen H. The role of biomarkers in the diagnosis and treatment follow-up of idiopathic pulmonary fibrosis. Sarcoidosis Vasc Diffuse Lung Dis. 2024;41:e2024015. 10.36141/svdld.v41i2.15454.
36. Majewski S, Szewczyk K, Żal A, Białas AJ, Miłkowska-Dymanowska J, Piotrowski WJ. Serial Measurements of Circulating KL-6, SP-D, MMP-7, CA19-9, CA-125, CCL18, and Periostin in Patients with Idiopathic Pulmonary Fibrosis Receiving Antifibrotic Therapy: An Exploratory Study. J Clin Med. 2021;10. 10.3390/jcm10173864.

37. Zhang B, Zhao D, Hu D. Induced sputum KL-6 combined with HRCT scoring for diagnosing and monitoring idiopathic pulmonary fibrosis. Biomol Biomed. 2025;26:452–61. 10.17305/bb.2025.12667.
38. Arshad HME, Ali F, Babar A, Raza MZ, Maqsood M, Ameer A. Survival impact and safety comparison of pirfenidone and nintedanib for idiopathic pulmonary fibrosis: A meta-analysis. Sarcoidosis Vasc Diffuse Lung Dis. 2025;42:16432. 10.36141/svdld.v42i3.16432.
39. Aribindi K, Liu GY, Albertson TE. Emerging pharmacological options in the treatment of idiopathic pulmonary fibrosis (IPF). Expert Rev Clin Pharmacol. 2024;17:817–35. 10.1080/17512433.2024.2396121.
40. Thannickal VJ, Roman J. Challenges in translating preclinical studies to effective drug therapies in idiopathic pulmonary fibrosis. Am J Respir Crit Care Med. 2010;181:532–3. 10.1164/rccm.200911-1740ED.
41. Yamada Z, Nishio J, Motomura K, Mizutani S, Yamada S, Mikami T, et al. Senescence of alveolar epithelial cells impacts initiation and chronic phases of murine fibrosing interstitial lung disease. Front Immunol. 2022;13:935114. 10.3389/fimmu.2022.935114.
42. Zhang T, Zhang J, Lv C, Li H, Song X. Senescent AEC and the implication for idiopathic pulmonary fibrosis treatment. Front Pharmacol. 2022;13:1059434. 10.3389/fphar.2022.1059434.
43. Yao C, Guan X, Carraro G, Parimon T, Liu X, Huang G, et al. Senescence of Alveolar Type 2 Cells Drives Progressive Pulmonary Fibrosis. Am J Respir Crit Care Med. 2021;203:707–17. 10.1164/rccm.202004-1274OC.
44. Han S, Lu Q, Liu X. Advances in cellular senescence in idiopathic pulmonary fibrosis (Review). Exp Ther Med. 2023;25:145. 10.3892/etm.2023.11844.
45. Ba J, Zheng C, Lai Y, He X, Pan Y, Zhao Y, et al. High matrix stiffness promotes senescence of type II alveolar epithelial cells by lysosomal degradation of lamin A/C in pulmonary fibrosis. Respir Res. 2025;26:128. 10.1186/s12931-025-03201-0.
46. Kim KK, Kugler MC, Wolters PJ, Robillard L, Galvez MG, Brumwell AN, et al. Alveolar epithelial cell mesenchymal transition develops in vivo during pulmonary fibrosis and is regulated by the extracellular matrix. Proc Natl Acad Sci U S A. 2006;103:13180–5. 10.1073/pnas.0605669103.
47. Chan TA, Hermeking H, Lengauer C, Kinzler KW, Vogelstein B. 14-3-3σ is required to prevent mitotic catastrophe after DNA damage. Nature. 1999;401:616–20. 10.1038/44188.
48. Yang HY, Wen YY, Chen CH, Lozano G, Lee MH. 14-3-3 sigma positively regulates p53 and suppresses tumor growth. Mol Cell Biol. 2003;23:7096–107. 10.1128/mcb.23.20.7096-7107.2003.
49. Falcicchio M, Ward JA, Chothia SY, Basran J, Mohindra A, Macip S, et al. Cooperative stabilisation of 14-3-3σ protein-protein interactions via covalent protein modification. Chem Sci. 2021;12:12985–92. 10.1039/d1sc02120f.
50. Song J, Liu Y, Liu F, Zhang L, Li G, Yuan C, et al. The 14-3-3σ protein promotes HCC anoikis resistance by inhibiting EGFR degradation and thereby activating the EGFR-dependent ERK1/2 signaling pathway. Theranostics. 2021;11:996–1015. 10.7150/thno.51646.

51. Du N, Li D, Zhao W, Liu Y. Stratifin (SFN) Regulates Cervical Cancer Cell Proliferation, Apoptosis, and Cytoskeletal Remodeling and Metastasis Progression Through LIMK2/Cofilin Signaling. Mol Biotechnol. 2024;66:3369–81. 10.1007/s12033-023-00946-1.
52. Banelli B, Bonassi S, Casciano I, Mazzocco K, Di Vinci A, Scaruffi P, et al. Outcome prediction and risk assessment by quantitative pyrosequencing methylation analysis of the SFN gene in advanced stage, high-risk, neuroblastic tumor patients. Int J Cancer. 2010;126:656–68. 10.1002/ijc.24768.
53. Aljabal G, Yap BK. 14-3-3σ and Its Modulators in Cancer. Pharmaceuticals (Basel). 2020;13. 10.3390/ph13120441.
54. Meng S, Arbit T, Veeriah S, Mellinghoff IK, Fang F, Vivanco I, et al. 14-3-3sigma and p21 synergize to determine DNA damage response following Chk2 inhibition. Cell Cycle. 2009;8:2238–46. 10.4161/cc.8.14.8998.
55. Chan TA, Hermeking H, Lengauer C, Kinzler KW, Vogelstein B. 14-3-3Sigma is required to prevent mitotic catastrophe after DNA damage. Nature. 1999;401:616–20. 10.1038/44188.

Figures

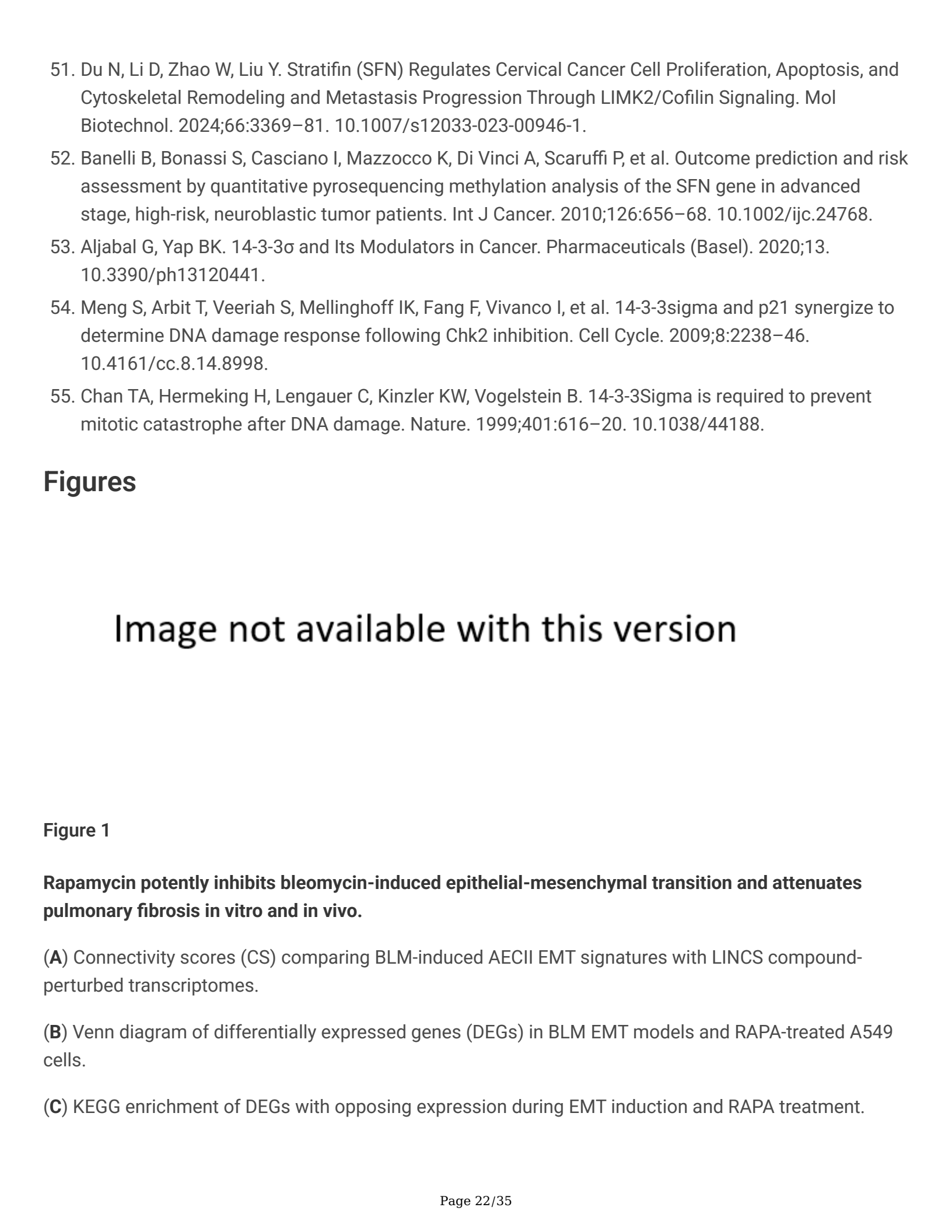


Figure 1

Rapamycin potently inhibits bleomycin-induced epithelial-mesenchymal transition and attenuates pulmonary fibrosis in vitro and in vivo.

(**A**) Connectivity scores (CS) comparing BLM-induced AECII EMT signatures with LINCS compound-perturbed transcriptomes.

(**B**) Venn diagram of differentially expressed genes (DEGs) in BLM EMT models and RAPA-treated A549 cells.

(**C**) KEGG enrichment of DEGs with opposing expression during EMT induction and RAPA treatment.

(**D**) Immunofluorescence for vimentin (green) and α-SMA (red) in A549 cells after 72 h treatment; nuclei counterstained with Hoechst (blue). 200× magnification (cropped view), scale bar = 5μm. Quantified fluorescence intensity analyzed via one-way ANOVA (n = 3).

(**E**) Western blot of vimentin and α-SMA in A549 cells at 24, 48, 72 h post-treatment. Band gray values analyzed via two-way ANOVA (n = 3).

(**F**) Relative Fibronectin and *ZO-1* mRNA levels at indicated time points. Data analyzed via two-way ANOVA (n = 3).

(**G**) Schematic timeline of in vivo mouse experiments.

(**H**) Kaplan–Meier survival curves for BLM-challenged mice ± RAPA, analyzed by log-rank test (n = 10).

(**I**) Lung *Col1a1*, *Tgfb1*, *E-cadherin* and *Vim* relative mRNA expression, analyzed via one-way ANOVA (n = 6).

(**J**) Representative H&E-stained lung sections; images captured at 200× (scale bar = 100 μm) or 400× (scale bar = 50 μm), as indicated on each panel (n = 6).

(**K**) Representative Masson's trichrome-stained lung sections; images captured at 200× (scale bar = 100 μm) or 400× (scale bar = 50 μm), as indicated on each panel (n = 6).

Data are shown as mean ± SEM. *p < 0.05, **p < 0.01, ***p < 0.001, ****p < 0.0001. All statistical tests were two-sided.

Figure 2

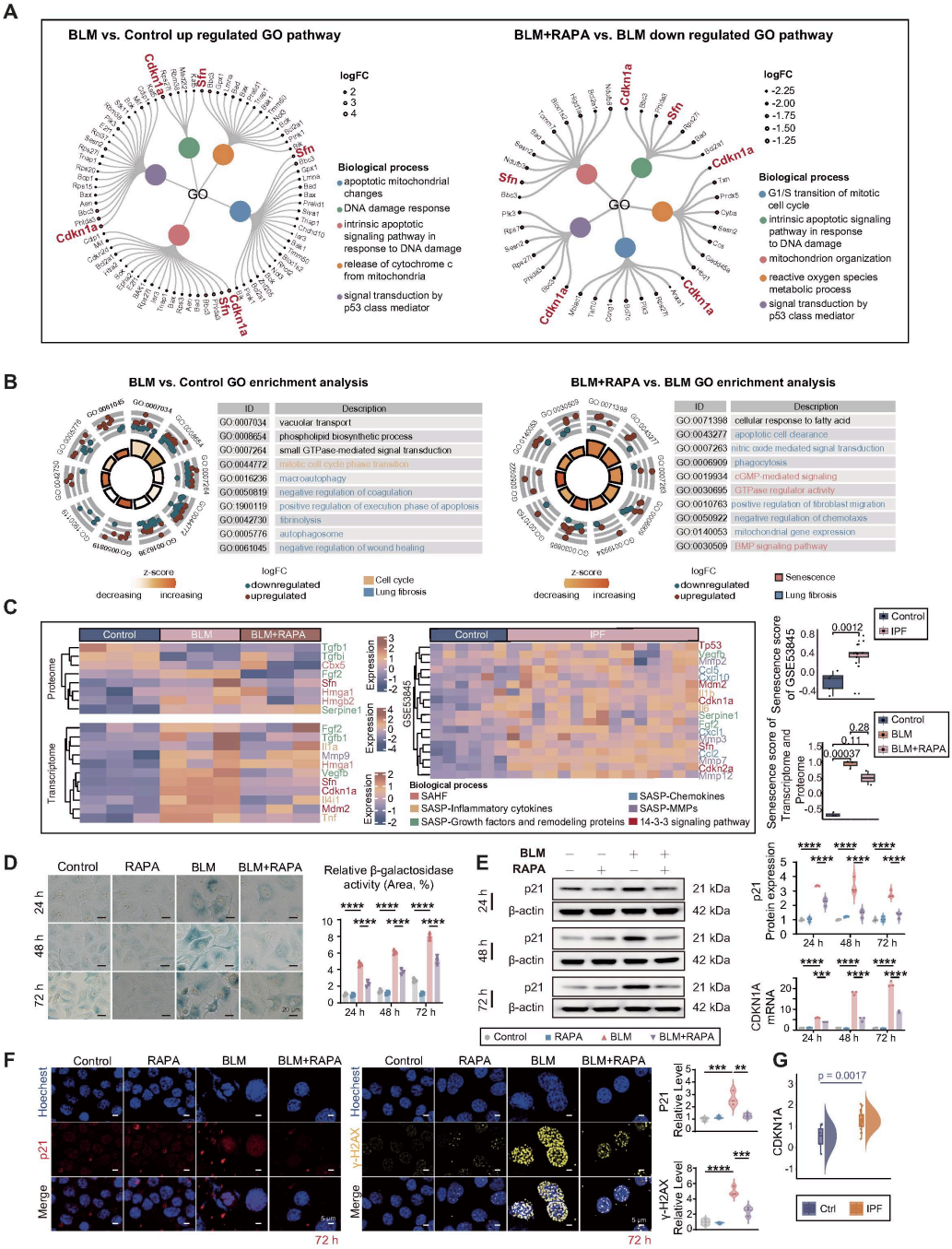


Figure 2

Rapamycin attenuates pulmonary fibrosis by suppressing AECII senescence identified via multi-omics.

(**A**) GO enrichment analysis of DEGs from lung tissue transcriptomes of indicated groups.

(**B**) GO enrichment analysis of differentially expressed proteins (DEPs) from proteomic profiling.

(**C**) Senescence scores and senescence-related gene heatmaps of mouse fibrotic lungs and human IPF dataset GSE53845.

(**D**) Representative SA-β-gal staining of treated A549 cells. 200× magnification (cropped view), scale bar = 20 μm. Staining positive rates analyzed via two-way ANOVA (n = 3).

(**E**) Western blot for p21 and relative *CDKN1A* mRNA levels in A549 cells at 24, 48, 72 h post-treatment. Gray value and qPCR data analyzed via two-way ANOVA (n = 3).

(**F**) Immunofluorescence for p21 (red) and γH2AX (yellow) in A549 cells after 72 h treatment; nuclei counterstained with Hoechst (blue). 200× magnification (cropped view), scale bar = 5 μm. Fluorescence intensity quantified with one-way ANOVA (n = 3).

(**G**) Relative CDKN1A expression in healthy controls and IPF patients (GSE53845).

Data are shown as mean ± SEM. *p < 0.05, **p < 0.01, ***p < 0.001, ****p < 0.0001. All statistical tests were two-sided.

Figure 3

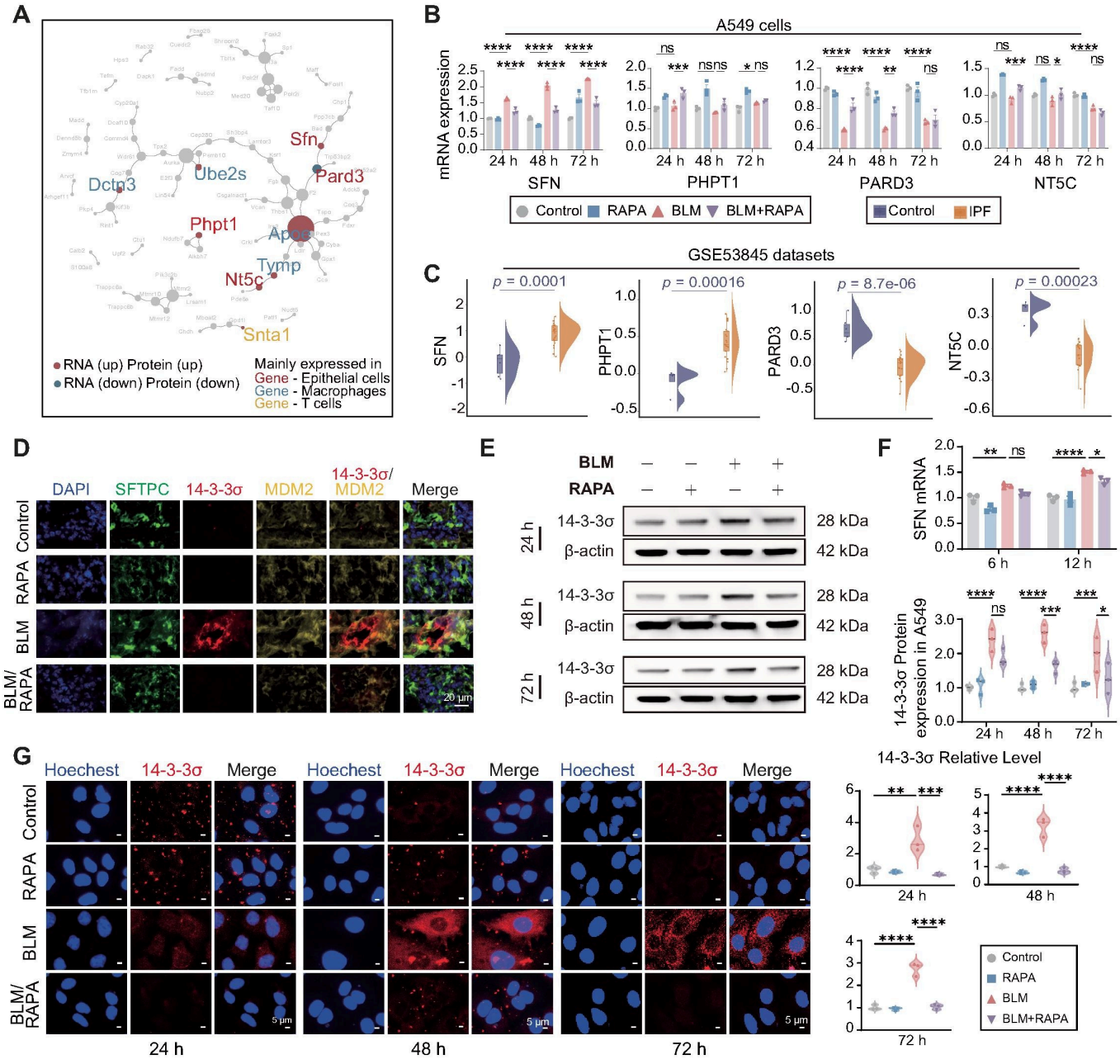


Figure 3

SFN (14-3-3σ) is identified as a key target mediating the anti-fibrotic effects of RAPA.

(**A**) Protein-protein interaction (PPI) network of DEGs between BLM-treated and control groups from multi-omics data.

(**B**) Relative *SFN*, *PHPT1*, *PARD3* and *NT5C* mRNA expression in A549 cells at 24, 48, 72 h post-treatment. Analyzed via two-way ANOVA (n = 3).

(**C**) SFN, PHPT1, PARD3 and NT5C expression in lung tissues of IPF patients and healthy controls (GSE53845).

(**D**) Immunofluorescence co-staining for 14-3-3σ (red), SFTPC (green) and MDM2 (yellow) in mouse lung sections; nuclei counterstained with DAPI (blue). Images captured at 400× (cropped view), scale bar = 20 μm.

(**E**) Western blot detection of 14-3-3σ in A549 cells at 24, 48, 72 h post-treatment. Band gray values analyzed via two-way ANOVA (n = 3).

(**F**) Relative *SFN* mRNA levels in A549 cells at 6 and 12 h after BLM stimulation, reflecting early transcriptional induction. Analyzed via two-way ANOVA (n = 3).

(**G**) Immunofluorescence staining for 14-3-3σ (red) in A549 cells collected at 24, 48, 72 h post-treatment; nuclei counterstained with DAPI (blue). 200× magnification (cropped view), scale bar = 5 μm. Quantified fluorescence intensity analyzed via two-way ANOVA (n = 3).

Data are shown as mean ± SEM. *p < 0.05, **p < 0.01, ***p < 0.001, ****p < 0.0001. All statistical tests were two-sided.

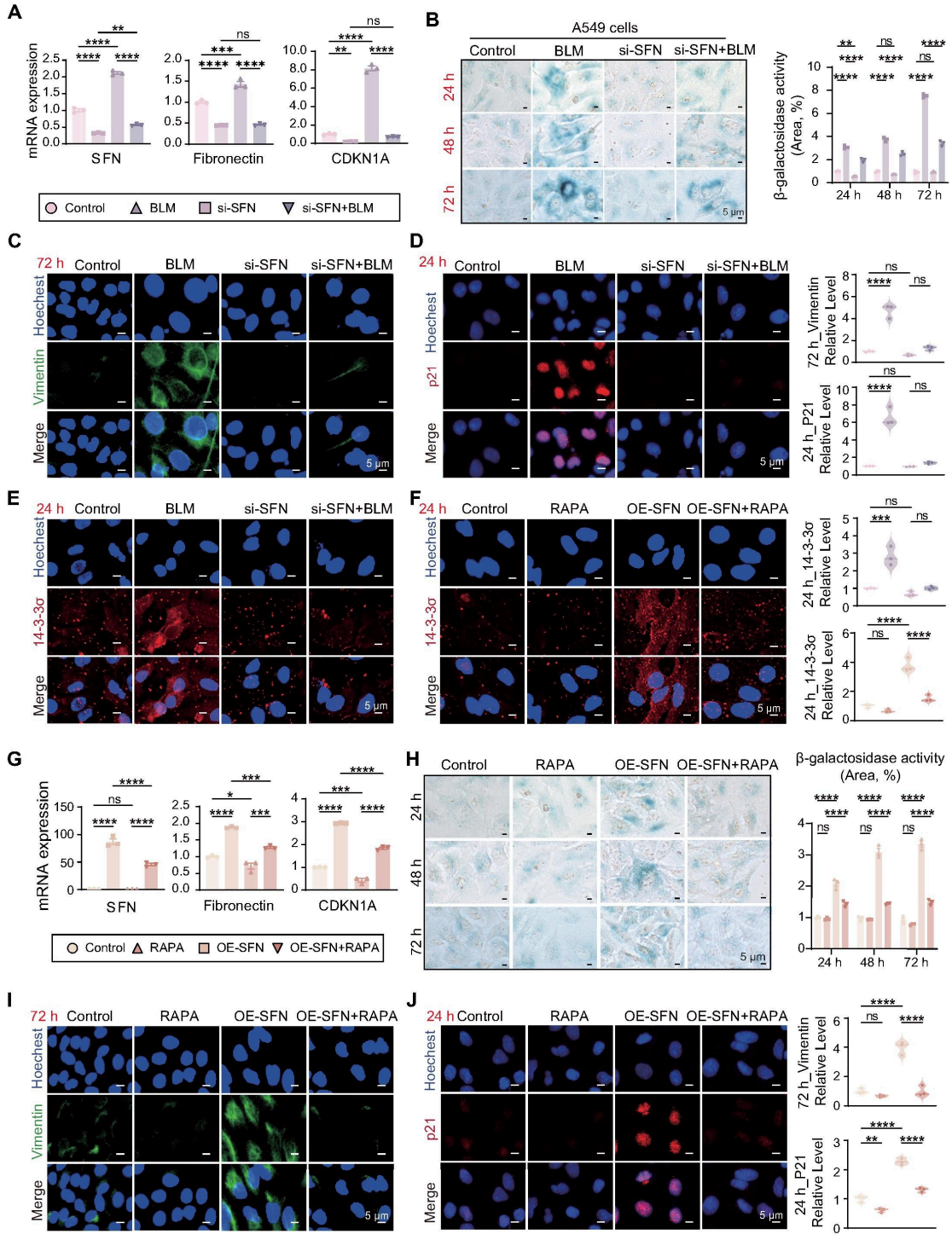


Figure 4

RAPA relieves BLM-induced AECII senescence and EMT via SFN.

(**A**) Relative *SFN*, *Fibronectin* and *CDKN1A* mRNA expression in *SFN*-knockdown A549 cells at 48 h post indicated treatments. Analyzed via one-way ANOVA (n = 3).

(**B**) Representative SA-β-gal staining for senescent *SFN*-knockdown A549 cells under distinct interventions. 400× magnification, scale bar = 5 μm. Positive cell rates quantified with two-way ANOVA (n = 3).

(**C**) Immunofluorescence for vimentin (green) in *SFN*-knockdown A549 cells at 72 h; nuclei counterstained with Hoechst (blue). 200× magnification (cropped view), scale bar = 5 μm. Fluorescence intensity analyzed via one-way ANOVA (n = 3).

(**D**) Immunofluorescence for p21 (red) in *SFN*-knockdown A549 cells at 24 h; nuclei counterstained with Hoechst (blue). 200× magnification (cropped view), scale bar = 5 μm. Fluorescence intensity analyzed via one-way ANOVA (n = 3).

(**E**) Immunofluorescence for 14-3-3σ (red) in *SFN*-knockdown A549 cells at 24 h post-treatment; nuclei counterstained with Hoechst (blue). 200× magnification (cropped view), scale bar = 5 μm. Fluorescence intensity analyzed via one -way ANOVA (n = 3).

(**F**) Immunofluorescence for 14-3-3σ (red) in *SFN*-overexpressing A549 cells at 24 h post-treatment; nuclei counterstained with Hoechst (blue). 200× magnification (cropped view), scale bar = 5 μm. Fluorescence intensity analyzed via one-way ANOVA (n = 3).

(**G**) Relative *SFN*, *Fibronectin* and *CDKN1A* mRNA expression in *SFN*-overexpressing rescue cells at 48 h post indicated treatments. Analyzed via two-way ANOVA (n = 3).

(**H**) Representative SA-β-gal staining for senescent *SFN*-overexpressing A549 cells under distinct interventions. 200× magnification, scale bar = 5 μm. Positive cell rates quantified with two-way ANOVA (n = 3).

(**I**) Immunofluorescence for vimentin (green) in *SFN*-overexpressing A549 cells at 72 h; nuclei counterstained with Hoechst (blue). 200× magnification (cropped view), scale bar = 5 μm. Fluorescence intensity analyzed via one-way ANOVA (n = 3).

(**J**) Immunofluorescence for p21 (red) in *SFN*-overexpressing A549 cells at 24 h; nuclei counterstained with Hoechst (blue). 200× magnification (cropped view), scale bar = 5 μm. Fluorescence intensity analyzed via one-way ANOVA (n = 3).

Data are shown as mean ± SEM. *p < 0.05, **p < 0.01, ***p < 0.001, ****p < 0.0001. All statistical tests were two-sided.

Figure 5

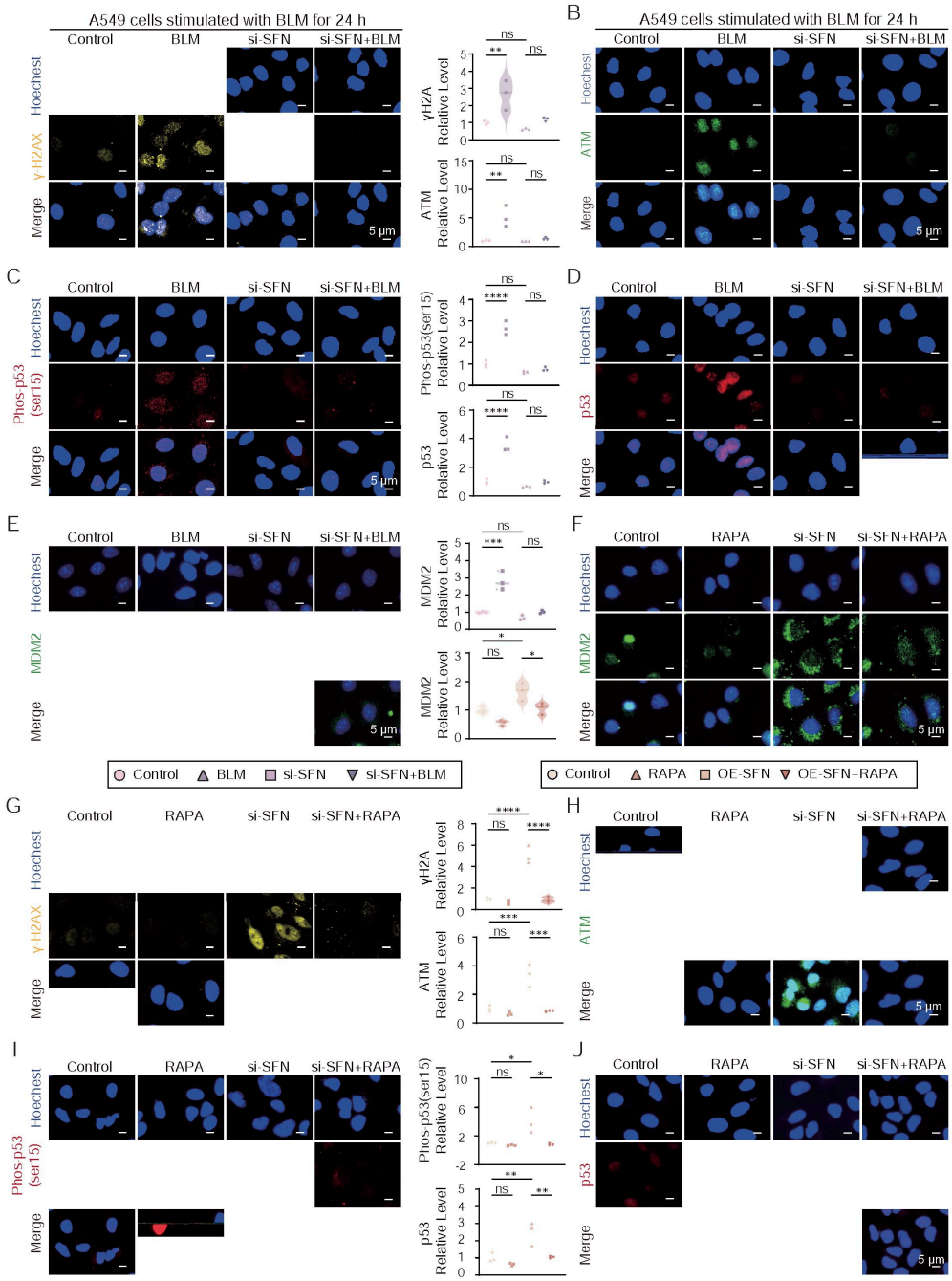


Figure 5

***SFN* regulates p53 signaling and DNA damage-dependent p53 activation.**

(**A and G**) Immunofluorescence staining for γH2AX (yellow) in *SFN*-knockdown and *SFN*-overexpression-rescued A549 cells at 24 h post-treatment; nuclei were counterstained with Hoechst (blue). 200×

magnification (cropped view), scale bar = 5 μm. Fluorescence intensity quantified via one-way ANOVA (n = 3).

(**B and H**) Immunofluorescence staining for ATM (green) in *SFN*-knockdown and *SFN*-overexpression-rescued A549 cells at 24 h post-treatment; nuclei were counterstained with Hoechst (blue). 200× magnification (cropped view), scale bar = 5 μm. Fluorescence intensity quantified via one-way ANOVA (n = 3).

(**C and I**) Immunofluorescence staining for phospho-p53 (Ser15) (red) in *SFN*-knockdown and *SFN*-overexpression-rescued A549 cells at 24 h post-treatment; nuclei were counterstained with Hoechst (blue). 200× magnification (cropped view), scale bar = 5 μm. Fluorescence intensity quantified via one-way ANOVA (n = 3).

(**D and J**) Immunofluorescence staining for p53 (red) in *SFN*-knockdown and *SFN*-overexpression-rescued A549 cells at 24 h post-treatment; nuclei were counterstained with Hoechst (blue). 200× magnification (cropped view), scale bar = 5 μm. Fluorescence intensity quantified via one-way ANOVA (n = 3).

(**E and F**) Immunofluorescence staining for MDM2 (green) in *SFN*-knockdown and *SFN*-overexpression-rescued A549 cells at 24 h post-treatment; nuclei were counterstained with Hoechst (blue). 200× magnification (cropped view), scale bar = 5 μm. Fluorescence intensity quantified via one-way ANOVA (n = 3).

Data are shown as mean ± SEM. *p < 0.05, **p < 0.01, ***p < 0.001, ****p < 0.0001. All statistical tests were two-sided.

Figure 6

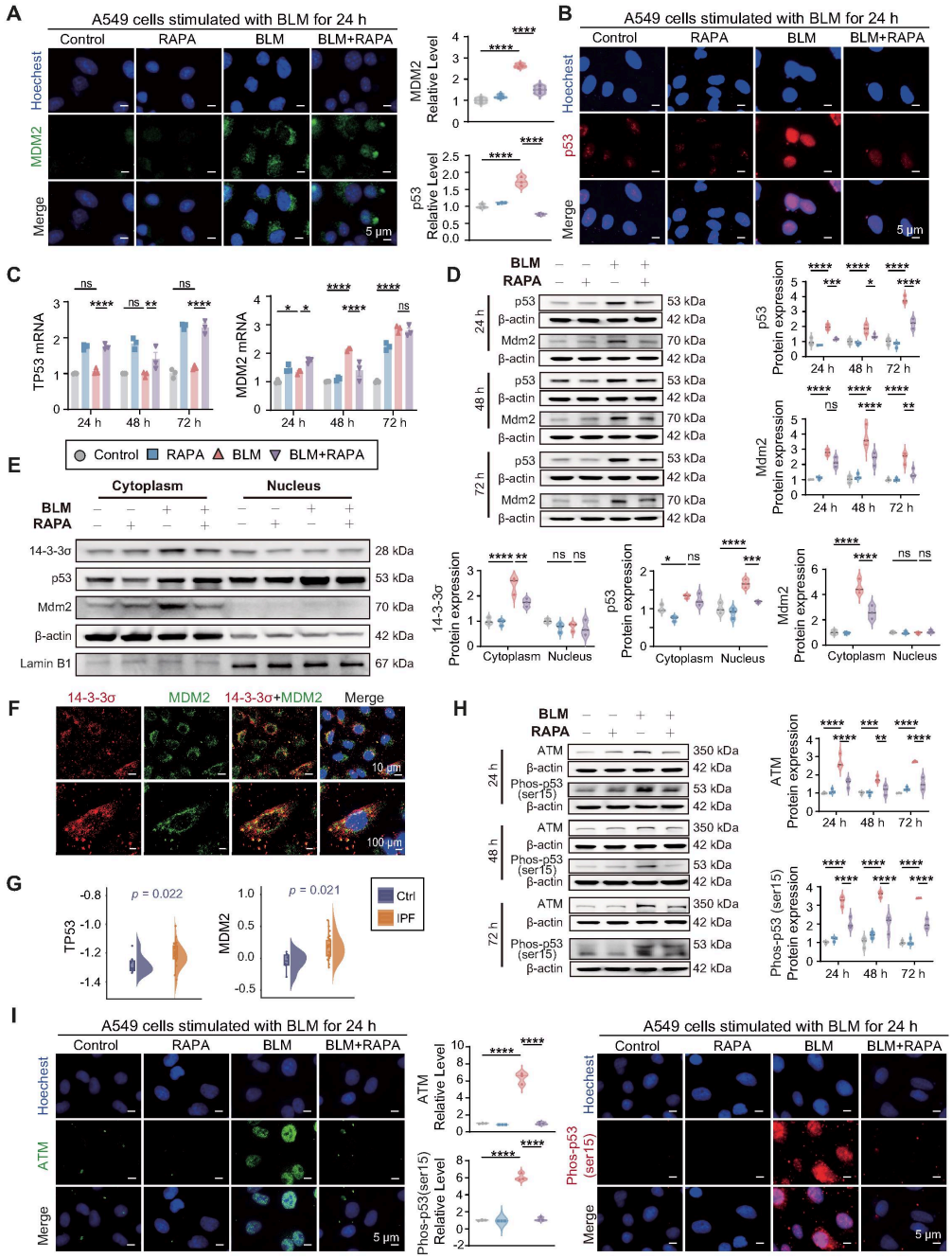


Figure 6

RAPA reverses BLM-induced activation of the MDM2/p53 signaling axis and ATM-mediated DNA damage signaling.

(**A**) Immunofluorescence staining for MDM2 (green) in A549 cells following 24 h of different treatments; nuclei counterstained with Hoechst (blue). 200× magnification (cropped view), scale bar = 5 μm.

Fluorescence intensity analyzed via one-way ANOVA (n = 3).

(**B**) Immunofluorescence staining for p53 (red) in A549 cells following 24 h of different treatments; nuclei counterstained with Hoechst (blue). 200× magnification (cropped view), scale bar = 5 μm. Fluorescence intensity analyzed via one-way ANOVA (n = 3).

(**C**) Relative *TP53* and *MDM2* mRNA expression in A549 cells at 24, 48, and 72 h post drug treatment. Analyzed via two-way ANOVA (n = 3).

(**D**) Western blot detection of total p53, and Mdmd2 protein levels in A549 cells at 24, 48, and 72 h post drug treatment. Band gray values analyzed via two-way ANOVA (n = 3).

(**E**) Western blot detection of 14-3-3σ, total p53, and Mdm2 protein levels in the cytoplasmic and nuclear fractions of A549 cells at 48 h post-drug treatment. Band gray values were analyzed using two-way ANOVA (n = 3).

(**F**) Immunofluorescence co-localization analysis of 14-3-3σ (red) and MDM2 (green) in A549 cells after 72 h of BLM stimulation; nuclei counterstained with Hoechst (blue). 200× magnification (cropped view), scale bar = 5 μm (n = 3).

(**G**) Relative TP53 and MDM2 expression in lung tissues from IPF patients and healthy controls (GSE53845).

(**H**) Western blot detection of ATM and Phos-p53 (ser15) protein levels in A549 cells at 24, 48, and 72 h post drug treatment. Band gray values analyzed via two-way ANOVA (n = 3).

(**I**) Immunofluorescence staining for ATM (green) and phospho-p53 (Ser15) (red) in A549 cells following 24 h of different treatments; nuclei counterstained with Hoechst (blue). 200× magnification (cropped view), scale bar = 5 μm. Fluorescence intensity analyzed via one-way ANOVA (n = 3).

Data are shown as mean ± SEM. *p < 0.05, **p < 0.01, ***p < 0.001, ****p < 0.0001. All statistical tests were two-sided.

Figure 7

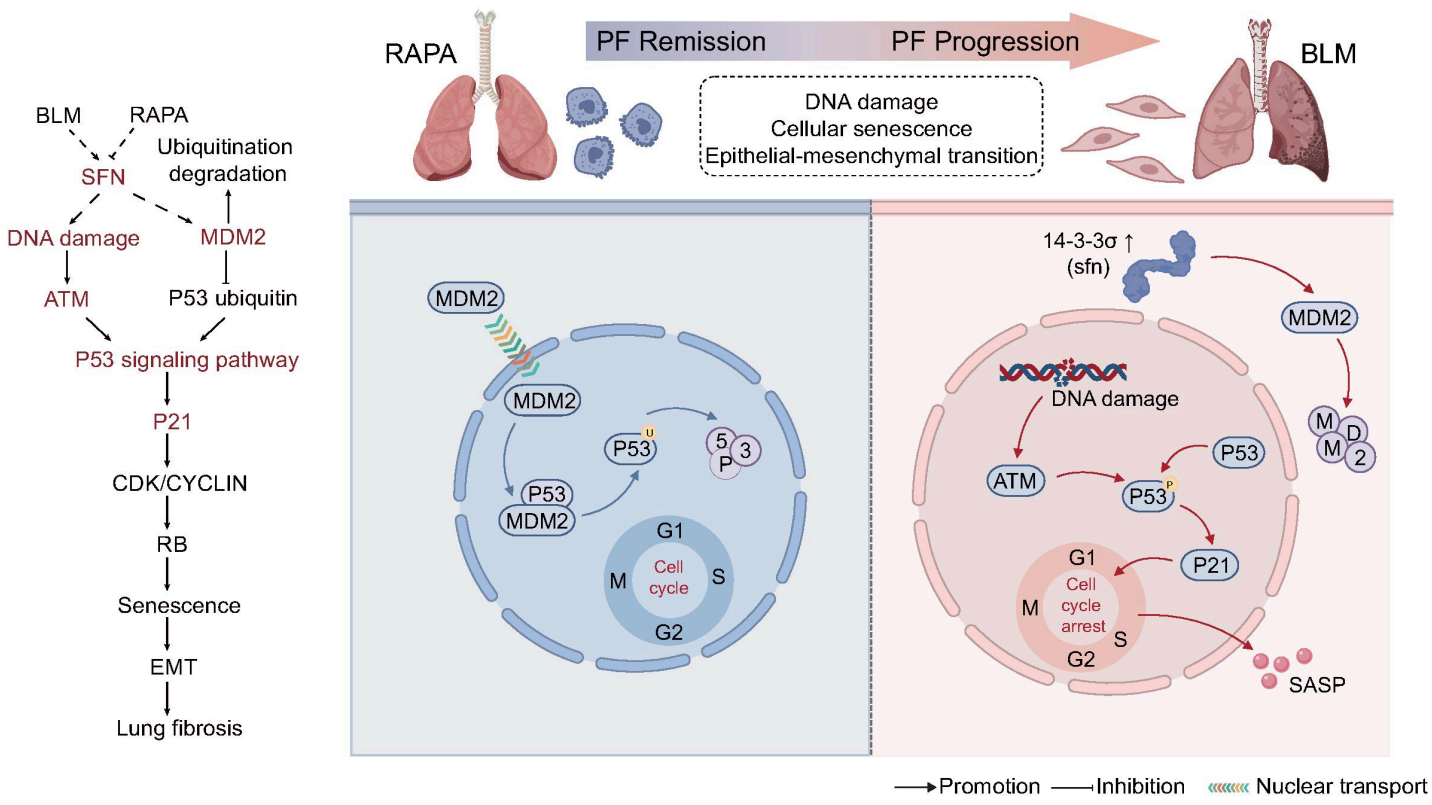


Figure 7

Schematic illustration of SFN/14-3-3σ mediating the anti-fibrotic and anti-senescent effects of rapamycin in BLM-induced pulmonary fibrosis.

In healthy alveolar epithelial cells, the SFN/14-3-3σ-MDM2-p53 pathway maintains cell cycle homeostasis. In BLM-induced pulmonary fibrosis, persistent DNA damage activates ATM-p53 signaling. BLM also upregulates SFN/14-3-3σ, which sequesters MDM2 in the cytoplasm, preventing p53 ubiquitination and degradation. Stabilized nuclear p53 induces p21, triggering cell cycle arrest, senescence, SASP release, and EMT, driving fibrosis progression. RAPA reverses this cascade: it downregulates SFN/14-3-3σ, restoring MDM2-p53 interaction and p53 turnover. Attenuated p53 signaling alleviates senescence, SASP, and EMT, thereby suppressing BLM-induced pulmonary fibrosis.

Supplementary Files

This is a list of supplementary files associated with this preprint. Click to download.

- SupplementaryWBRawImagesrelatedtoFig.1.pdf

- SupplementaryWBRawImagesrelatedtoFig.2.pdf
- SupplementaryWBRawImagesrelatedtoFig.3.pdf
- SupplementaryWBRawImagesrelatedtoFig.61.pdf
- SupplementaryWBRawImagesrelatedtoFig.62.pdf
- SupplementaryWBRawImagesrelatedtoFig.63.pdf
- SupplementaryWBRawImagesrelatedtoFig.64.pdf
- SupplementaryWBRawImagesrelatedtoFig.65.pdf
- SupplementaryTranscriptome.fpkm.csv
- SupplementaryTablesFigures.pdf
- SupplementaryProteomeLFQ.csv